Front. Phys., 2014, 9(1): 47–59
DOI 10.1007/s11467-013-0357-1

REVIEW ARTICLE

Oblique angle deposition and its applications in plasmonics

Yizhuo He[1], **Junxue Fu**[2], **Yiping Zhao**[1,†]

[1] *Department of Physics and Astronomy, and Nanoscale Science and Engineering Center, University of Georgia, Athens, Georgia 30602, USA*

[2] *Department of Physics, Hong Kong Baptist University, Kowloon Tong, Hong Kong, China*

Corresponding author. E-mail: †*zhaoy@physast.uga.edu*

Received April 19, 2013; accepted May 29, 2013

Plasmonics based on localized surface plasmon resonance (LSPR) has found many exciting applications recently. Those applications usually require a good morphological and structural control of metallic nanostructures. Oblique angle deposition (OAD) has been demonstrated as a powerful technique for various plasmonic applications due to its advantages in controlling the size, shape, and composition of metallic nanostructures. In this review, we focus on the fabrication of metallic nanostructures by OAD and their applications in plasmonics. After a brief introduction to OAD technique, recent progress of applying OAD in fabricating noble metallic nanostructures for LSPR sensing, surface-enhanced Raman scattering, surface-enhanced infrared absorption, metal-enhanced fluorescence, and metamaterials, and their corresponding properties are reviewed. The future requirements for OAD plasmonics applications are also discussed.

Keywords Oblique angle deposition, glancing angle deposition, Plasmonics, localized surface plasmon resonance, surface-enhanced Raman spectroscopy, surface-enhanced infrared absorption, metal-enhanced fluorescence, metamaterial

PACS numbers 81.07.-b, 73.22.Lp, 78.67.-n, 73.20.Mf

Contents

1 Introduction

Plasmonics is a rapidly growing research field, which explores the optical properties of metallic nanostructures, and inspires many applications from novel materials design to biomedical diagnostics. Plasmonics include two distinct phenomena: surface plasmon resonance (SPR) and localized surface plasmon resonance (LSPR). For thin noble metallic films, when electromagnetic (EM) waves interacts with the metallic surface, it will generate charge density wave, and at certain wavelength or incident geometry, when the horizontal component of the incident wavevector matches with the intrinsic wavevector of the charge density wave, a resonance absorbance will occur, which is referred to as SPR. For individual metallic nanostructures, similar resonance absorbance due to confined collective oscillation of electrons in the nanostructure can be observed, and is referred to as LSPR. The LSPR depends on the material, size, shape, and also the surrounding dielectric environment [1–3], and has been widely applied for chemical and biological sensing [4, 5]. The LSPR sensing utilizes the principle that the LSPR resonant wavelength depends on the dielectric constant of the surrounding. In addition, the enhanced localized EM fields generated by LSPR at the resonant wavelength are found to be the main origins for the surface-enhanced spectroscopies, such as surface-enhanced Raman spectroscopy (SERS) [6–8], surface-enhanced infrared absorption (SEIRA) [9, 10], and metal-enhanced fluorescence (MEF) [11–13]. Moreover, LSPR has been utilized to engineer the electromagnetic properties of metamaterials due to their strong EM coupling in sub-wavelength region [14, 15], which possess unique properties usually not found in nature.

Frontiers of Physics

One important aspect with various plasmonic applications is to tune the LSPR properties by precisely controlling the morphology of the metallic nanostructures. For example, in SERS, the LSPR wavelength of the metallic substrates needs to be designed close to the excitation wavelength to achieve high enhancement. In addition, practical applications also require the nanostructures to be uniform, reproducible, low-cost, and easy to fabricate. A great deal of efforts have been devoted to the fabrication of various metallic nanostructures for plasmonic applications. Many of them require nanostructures supported on substrates. This imposes a great challenge to the fabrication techniques. Methods that can directly fabricate nanostructures on substrates are usually used, such as lithography methods [16, 17], self-assembly methods [18], and physical vapor deposition (PVD) methods [19–21]. Electron beam lithography (EBL) is an ideal method for fabricating regular nanostructures for plasmonic applications due to its ability to precisely control the size, shape, and spacing of the nanostructures [22–25]. But EBL is expensive, time-consuming, and thus not suitable for scalable fabrication. As a cheap and simple technique, nanosphere lithography (NSL) [26–28], can easily produce two-dimensional well-ordered nanoparticle arrays, but has the poor ability to tune the shape of naonstructures and to achieve large surface area. Self-assembled metallic colloid is another popular way to produce ordered nanostructures [18]. The monolayer of colloid can be formed by reduction reaction, while the random aggregation can often occur, leading to a poor uniformity and reproducibility. Physical vapor deposition methods, such as electron-beam deposition, sputtering growth, and thermal evaporation, are commonly used to fabricate large-scale thin films. With a normal vapor incidence with respect to the substrates, nanoparticles or thin films are generally formed on the substrates. When the vapor is incident with a large angle ($\theta > 70°$) with respect to the surface normal of substrates, nanocolumns are usually formed. This kind of physical vapor deposition with large incident angles is referred to as oblique angle deposition (OAD) [29].

The principle of OAD is shown in Fig. 1(a). The incident vapor flux is arriving at the substrate at an angle θ, which can be tuned by changing the orientation of substrates through a stepper motor. A quartz crystal microbalance (QCM) is usually used to monitor the deposition thickness, which is referred to as QCM thickness t_{QCM}. In OAD, the geometric shadowing effect and surface diffusion of the adatoms account for the formation of the nanostructures [29, 30]. At the beginning of the deposition, islands with different heights are randomly formed on the substrates. As the deposition proceeds, the shorter islands will be shadowed by the nearby taller ones and cannot receive more vapor atoms; while the taller islands continuously receive the source atoms and grow longer. In the meantime, the adatoms move on the surface due to the surface diffusion. Consequently, a layer of nanocolumns tilted towards the direction of incident vapor is formed. Four structural parameters are usually used to describe the structure of an OAD nanocolumn layer: the tilting angle β, the length l, the diameter D, and the density ρ of the nanocolumns as shown in Fig. 1(b). By adjusting the deposition parameters, the morphology of nanocolumns can be changed. The qualitative relationship between the deposition parameters and the structural parameters is listed in Table 1.

As the extension of OAD technique, glancing angle deposition (GLAD) is a combination of OAD and the azimuthal rotation of the substrate [21]. An additional motor which controls the azimuthal motion of the substrate is added to the deposition system. By programing the substrate's polar and azimuthal rotations, a large variety of morphologies of nanostructures can be fabricated. For example, vertical aligned nanorods can be fabricated

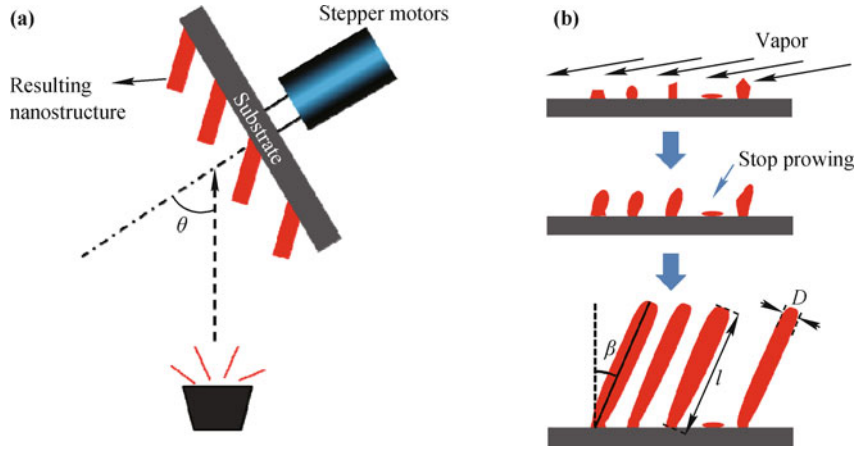

Fig. 1 **(a)** The schematics of OAD and GLAD, and **(b)** the self-shadowing effect during growth.

Table 1 The relationship between the deposition parameters and the structural parameters.

Deposition parameters	Structural parameters			
	Diameter D	Length l	Tilting angle β	Density ρ
Incident angle $\theta \uparrow$	-	-	$\uparrow$	$\downarrow$
QCM thickness $t_{\mathrm{QCM}} \uparrow$	$\uparrow$	$\uparrow$	-	$\downarrow$
Substrate temperature $T \uparrow$	$\uparrow$	$\downarrow$	$\downarrow$	-

by fixing the incident angle and rotating the substrate azimuthally at a fast speed during the deposition; helical nanostructures can be obtained by using a slow azimuthal rotation speed; and so on [21, 31, 32]. Besides the diverse shape of nanostructures, different materials can be used in OAD and GLAD as long as they can be evaporated. By combining the morphological design and the depositions of different materials, composite and heterogeneous nanostructures have been realized [33, 34]. The composite-nanostructures can be fabricated through a co-deposition, in which two or more materials are vaporized and deposited on the substrates simultaneously [35–39], while the heterogeneous nanostructures can be obtained through a series of depositions of different materials [40–43]. So far, OAD and GLAD have been demonstrated as powerful fabrication techniques and have the following merits: (i) different size, shape and morphology of nanocolumns can be obtained by conveniently changing the deposition parameters such as incident angle θ, QCM thickness t_{QCM}, substrate temperature T, and substrate azimuthal rotation ϕ; (ii) the materials of nanostructures are not limited as long as it can be evaporated; (iii) nanostructures are self-aligned on the substrate; and (iv) the cost is low and large-area fabrication is feasible. The metallic nanostructures made by OAD and GLAD have been used for various plasmonic applications such as LSPR sensors, SERS, SEIRA, MEF, and metamaterials. Some of the applications have demonstrated excellent performance. In the following sections, we will discuss those applications based on the plasmonic nanostructures fabricated by OAD and GLAD.

2 Localized surface plasmon resonance sensors

Ultra-thin layer of noble metallic nanoparticles (NPs) can be used to generate LSPR response. The LSPR wavelength is determined by the size, shape, and material of the nanoparticles as well as the dielectric environment. The dependence of LSPR on the surrounding environment can be utilized for sensor applications. By physical vapor deposition at a normal incident configuration, Ag and Au NP films can be fabricated and exhibit LSPR properties [44]. However, our study reveals that a small incident angle θ usually leads to a large variation in the nanoparticle size distribution and poor uniformity [45]. By using OAD and GLAD, narrower size distribution and more uniform Ag and Au NP films can be fabricated. Figures 2(a) and (b) show the representative atomic force microscope (AFM) images of Ag NP film ($t_{\mathrm{QCM}} = 25$ nm, $\theta = 85°$) and Au NP film ($t_{\mathrm{QCM}} = 10$ nm, $\theta = 85°$) fabricated by OAD, respectively. The Ag or Au films are composed of small and uniform NPs, whose corresponding LSPR peaks are located at 440 nm and 570 nm, respectively, as shown in Fig. 2(c). GLAD was also used to produce Ag or Au NPs films. The Au NPs deposited by GLAD with the same t_{QCM} have the similar morphology as that fabricated by OAD (image not shown) [46]. With a film thickness of 150 nm, the Ag NPs prepared by GLAD have a large size distribution, as shown in Fig. 2(d), with diameters ranging from approximately 20 to 300 nm [47].

The LSPR property of metallic NPs is typically characterized by examining the LSPR wavelength (LSPRW) λ_p and its response to the refractive index of the surrounding environment. From the Mie theory, the LSPRW λ_p red shifts with the increasing particle size, or film thickness [48, 49]. Figure 3(a) shows the λ_p–t_{QCM} relationship of Ag NPs fabricated by OAD with the increasing incident angles. The LSPRW λ_p has an averaged red shift of 2–10 nm per 1 nm increment in t_{QCM} at $\theta \geqslant 70°$, indicating that a fine tunability of LSPRW can be achieved by using OAD or GLAD.

To investigate the response of nanoparticles to the surrounding medium, the extinction spectra were measured by immersing the OAD Ag NP sample shown in Fig. 2(d) in deionized water, 2-propanol, and chloroform, with refractive indices of 1.33, 1.38, and 1.45, respectively, as shown in Fig. 3(b). The wavelength shift $\Delta\lambda_p$ was found to be linearly dependent on the refractive index with a sensitivity of 123 ± 3 nm/RIU (RIU represents refractive index unit) [47].

The LSPR properties of metal/insulator/metal island films deposited by OAD or GLAD have also been explored [46]. Au NPs/TiO_2 film/Au NPs sandwich structures were fabricated by GLAD and the normalized absorbance spectra of Au NPs, Au NPs/TiO_2 film, and Au

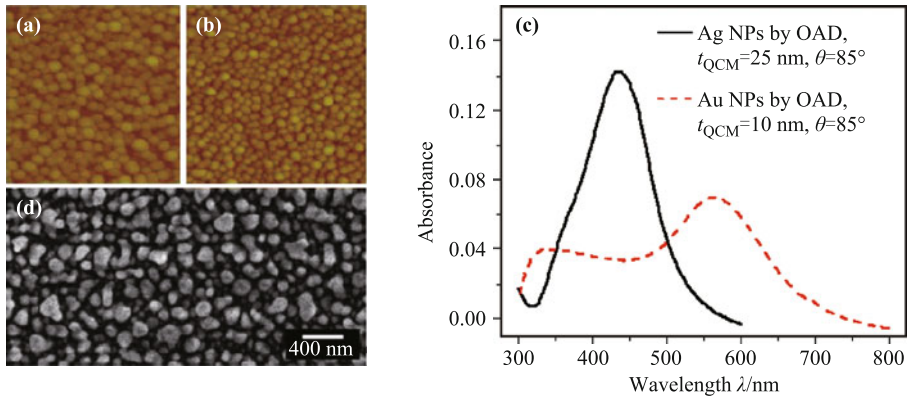

Fig. 2 Representative AFM images of **(a)** Ag NPs (t_{QCM} = 25 nm, θ = 85°) and **(b)** Au NPs (t_{QCM} = 10 nm, θ = 85°) films made by OAD. The scan length is 0.5 μm. **(c)** Absorbance spectra of samples in (a) and (b). **(d)** SEM image of Ag NPs (real thickness t = 150 nm, θ = 85°, the substrate is rotated azimuthally at a rate of one revolution for every 3 nm of film growth) fabricated by GLAD. (a) reproduced from Ref. [45], Copyright © 2008 American Chemical Society; (b) reproduced from Ref. [46], Copyright © 2010 Institute of Physics; (d) reproduced from Ref. [47], Copyright © 2007 American Chemical Society.

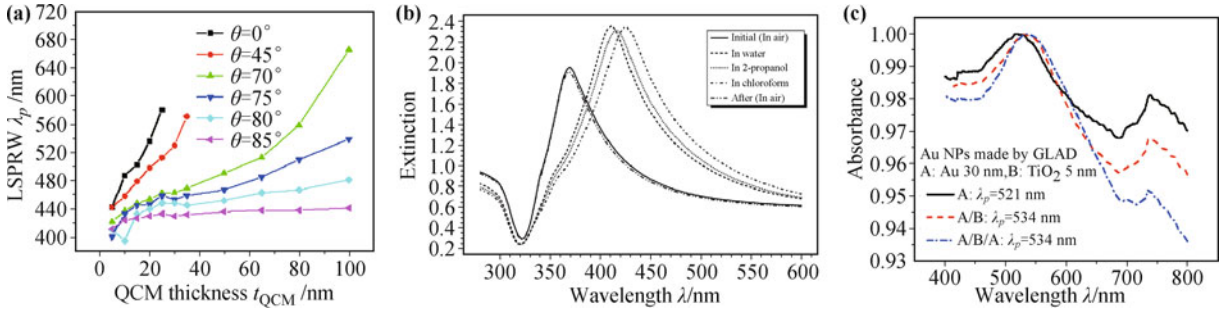

Fig. 3 **(a)** The relationship between λ_p and t_{QCM}. The measurements were performed on Ag NPs made by OAD. **(b)** Extinction spectra in air before solvent measurements, in solvents of varying index of refraction, and in air again after the solvent measurements. **(c)** Normalized absorbance spectra of substrates A, A/B and A/B/A. A: Au NPs made by GLAD (t_{QCM} = 30 nm). B: TiO_2 deposition by GLAD (t_{QCM} = 5 nm). (a) reproduced from Ref. [45], Copyright © 2008 American Chemical Society; (b) reproduced from Ref. [47], Copyright © 2007 American Chemical Society; (c) reproduced from Ref. [46], Copyright © 2010 Institute of Physics.

NPs/TiO_2 film/Au NPs are shown in Fig. 3(c). After a 5 nm TiO_2 coating, the plasmon peak of the Au NPs shifted from 521 nm to 534 nm, due to change in dielectric environment after the coating of TiO_2. Interestingly, after another layer of Au with the same thickness coating, the LSPRW did not shift, which means that the TiO_2 layer can act as a spacer between two Au NP depositions. This additional layer of TiO_2, like the bow-tie structure, could generate more "hot spots" for plasmonic applications.

The sensing ability of OAD Ag NPs based on LSPR principle to monitor the binding between biotin and NeutrAvidin has been demonstrated [45]. After a fresh Ag NPs film (t_{QCM} = 50 nm, θ = 85°) went through the biotin coating, bovine serum albumin (BSA) blocking and 10^{-6} M NeutrAvidin binding step, its LSPRW λ_p red shifted from 447 nm to 462 nm, 490 nm, and 509 nm, respectively. The change of λ_p from 490 nm to 509 nm was due to biotin-NeutrAvidin binding. Further, different concentration of NeutrAvidin was detected and a clear concentration dependence relationship is shown in Fig. 4(a), with a detection limit of NeutrAvidin of 10^{-10} M ($\Delta\lambda_p$ = 4 nm) [45]. The LSPR biosensing capability of Ag NPs films fabricated by GLAD has also been evaluated by detecting the binding event of anti-rabbit immunoglobulin G (anti-rIgG) to rabbit immunoglobulin G (rIgG) attached to the nanoparticle surface. Figure 4(b) shows the shift of LSPRW $\Delta\lambda_p$, versus anti-rIgG concentration, [anti-rIgG], with a detection limit of 27 nM ($\Delta\lambda_p$ = 2 nm) [47]. The above applications verify the sensing property of metallic nanoparticle films fabricated by OAD or GLAD for small molecule detection.

3 Surface-enhanced Raman scattering

SERS has become a powerful technique for chemical and biological sensing applications due to its great sensitivity.

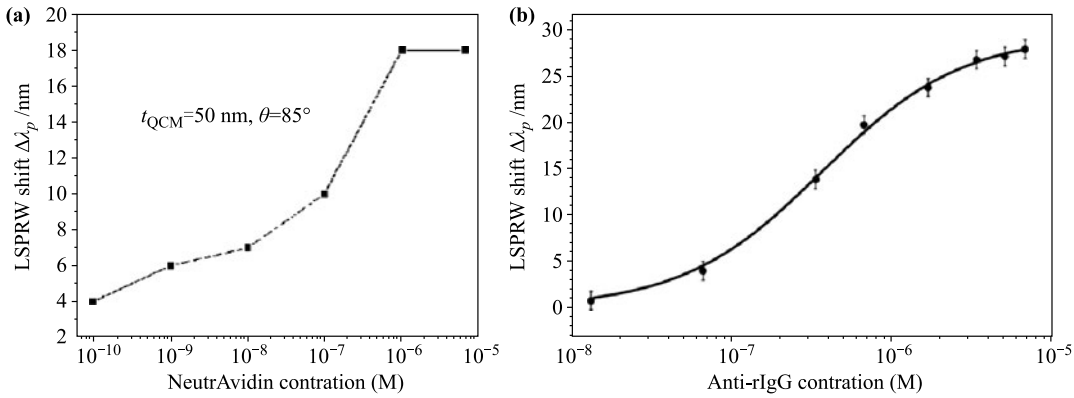

Fig. 4 **(a)** Concentration dependence of NeutrAvidin for SPRW shift $\Delta\lambda_p$ based on Ag NPs. **(b)** The LSPRW shift as a function of anti-rIgG concentration. (a) reproduced from Ref. [45], Copyright © 2008 American Chemical Society; (b) reproduced from Ref. [47], Copyright © 2007 American Chemical Society.

The application of SERS usually requires the substrates with good sensitivity and reproducibility. A variety of Ag nanostructures fabricated by OAD and GLAD techniques have been explored [19, 50–54] and some of them have demonstrated as excellent SERS substrates. Among these Ag nanostructures, tilted Ag nanorod (AgNR) arrays are simple to prepare by OAD, and have exhibited very good sensitivity and reproducibility [19, 50, 55, 56]. As shown in the SEM images in Figs. 5(a) and (b), a typical layer of AgNRs with QCM thickness $t_{QCM} = 2$ μm at an incident angle $\theta = 86°$ under room temperature (RT) is deposited on a 500 nm thick Ag film. The tilting angle β, nanorod length l, and diameter D of the resulting AgNRs are $71° \pm 4°$, 800–900 nm, and 100 nm, respectively. The SERS response of these AgNR substrates is characterized by measuring the Raman spectrum of trans-1,2-bis(4-pyridyl) ethylene (BPE) molecules adsorbed on AgNRs. The enhancement factor (EF), defined as the enhancement in SERS signal per molecule relative to the bulk Raman signal, is evaluated to be as high as 5×10^8. The uniformity and reproducibility of the AgNR substrates are also estimated by static measurement [50]: the point-to-point uniformity (relative standard deviation) in BPE SERS intensity obtained on a single substrate is about 10%; the substrate-to-substrate reproducibility within one batch ranges from 6% to 13%; and the batch-to-batch reproducibility is less than 15%. If a rotating detection scheme is used, the point-to-point uniformity is <5% [57]. Both the enhancement factor and reproducibility obtained on AgNR substrates fabricated by OAD are comparable to or even better than those of SERS substrates prepared by other techniques [58, 59].

As shown in Table 1, the structural parameters of the OAD AgNR arrays can be tuned by varying three deposition parameters, incident angle θ, QCM thickness t_{QCM}, and substrate temperature T, and thus the SERS activity may also be changed. The influence of QCM thickness and incident angle on the SERS activity has been

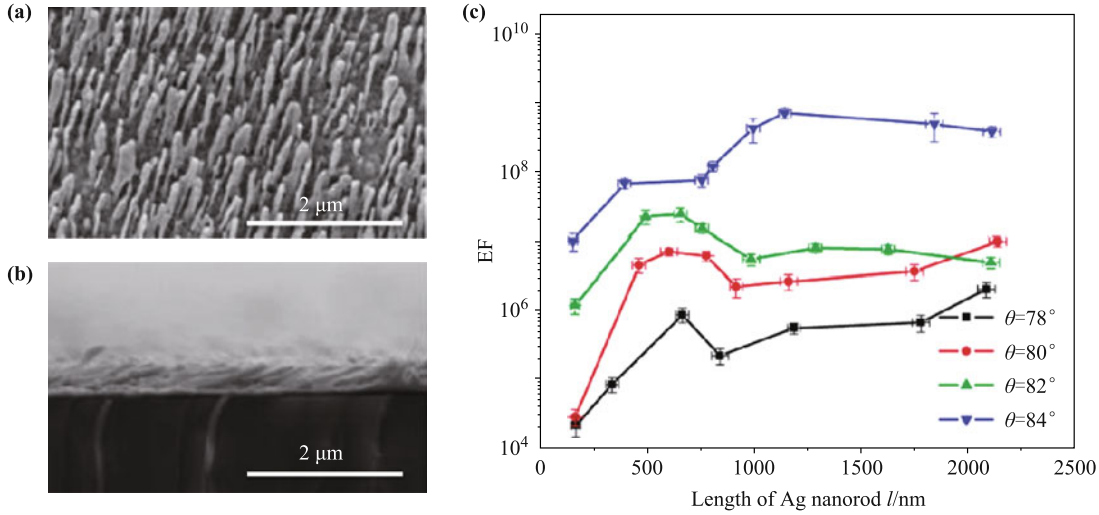

Fig. 5 **(a)** Top view and **(b)** cross-sectional SEM images of OAD AgNR arrays with $\theta = 86°$. **(c)** SERS EF vs nanorod length l with different incident angles θ. (a) and (b) reproduced from Ref. [50], Copyright © 2008 American Chemical Society; (c) reproduced from Ref. [19], Copyright © 2010 American Chemical Society.

investigated by Liu *et al.* [19] and Driskell *et al.* [50] under room temperature. In their study, AgNR arrays with various nanorod lengths l (= 200–2000 nm) and tilting angles β (= 57°, 61°, 63°, 65°, and 71°) were fabricated by OAD with varying QCM thickness t_{QCM} (= 400–4000 nm) and incident angles θ (= 78°, 80°, 82°, 84°, and 86°). Figure 5(c) shows the relationship between enhancement factor EF and nanorod length l at different incident angles θ. For different θ, the EF increases, reaches a maximum at an optimal nanorod length and then decreases, as l increases. A further increase in nanorod length l may result in an increase of EF for θ = 78° and 80°. From another aspect, EF generally increases with the incident angle θ, when the nanorod length l is fixed. As shown in Table 1, a smaller θ leads to larger density ρ of Ag nanorods, which increases the possibility that two or more adjacent Ag nanorods contact each other or fuse together. This could reduce the strength of the localized EM field and surface area, resulting smaller EF. Consequently, the optimal AgNR SERS substrate by OAD under RT can be achieved with incident angle θ = 86°. At this incident angle, the best SERS activity is obtained with $t_{\mathrm{QCM}} \approx 2$ μm [50].

Besides t_{QCM} and θ, the substrate temperature T can also affect the morphology of AgNR arrays and the SERS activity. Low-temperature (LT) deposition usually results in longer nanorods with smaller diameters since the low temperature limits the surface diffusion of Ag adatoms and increases the sticking coefficient of Ag, leading to an increase in the growth along nanorod and a decrease in the lateral growth. Singh *et al.* fabricated AgNR SERS substrates by OAD at low temperature T = 140 K [53]. As shown in the top-view and cross-sectional SEM images in Figs. 6(a) and (b), the AgNRs made at T = 140 K have larger nanorod length l and smaller diameter D than those prepared at RT under similar deposition conditions. In addition, there are many nano-sized pores on the AgNRs by LT OAD and blade-like structures are formed at the tips. The SERS activity is quantified by the SERS intensity of the band of BPE at 1200 cm^{-1} (I_{1200}), which corresponds to the in-plane ring mode of C=C. The dependence of both l and I_{1200} on t_{QCM} is shown in Figs. 6(c) and (d), respectively. The SERS substrate made by LT OAD with t_{QCM} = 550 nm exhibits highest SERS signal, and further increase in QCM thickness reduces the SERS activity. Surprisingly, the optimal SERS substrate made by RT OAD with t_{QCM} = 2 μm and θ = 86° only yields 60% of the SERS intensity I_{1200} obtained by the LT SERS substrate with t_{QCM} = 550 nm. To explain the high sensitivity of LT AgNRs, a finite difference time domain (FDTD) simulation was performed and indicated that the nano-size pores

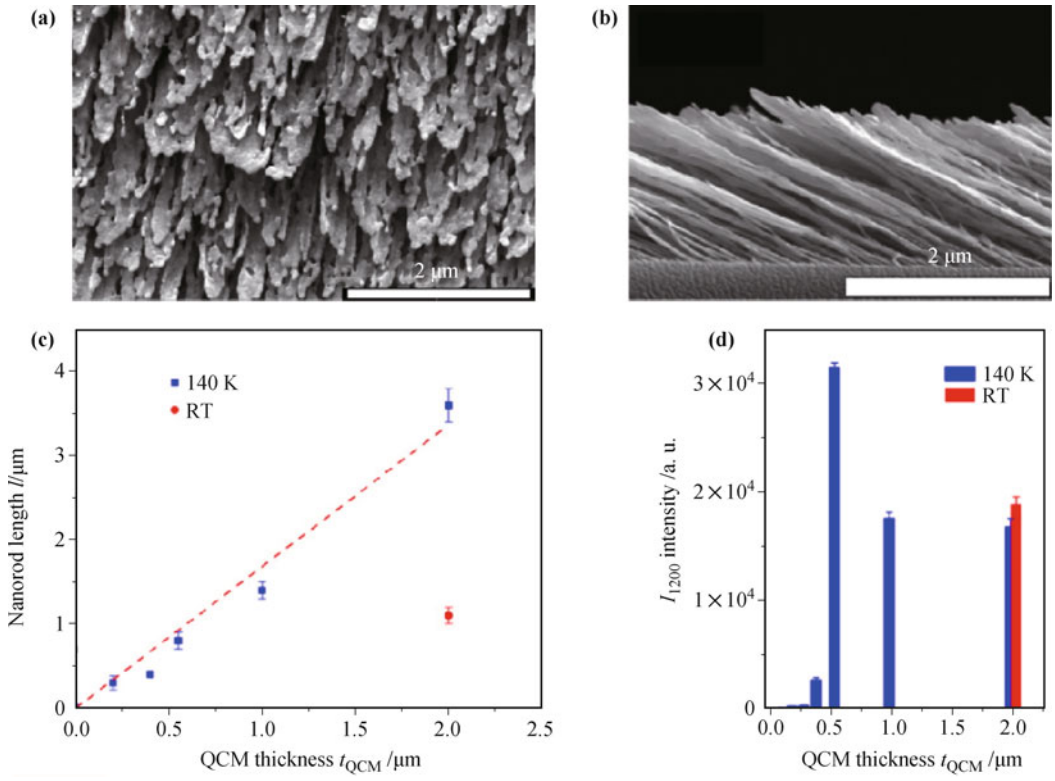

Fig. 6 **(a)** Top view and **(b)** cross-sectional SEM images of OAD AgNR arrays deposited at T = 140 K with θ = 86°. **(c)** Dependence of nanorod length l and **(d)** I_{1200} on t_{QCM} for AgNRs made at LT and RT. Reproduced from Ref. [53], Copyright © 2012 American Chemical Society.

and the blade-like connected rod tips played an important role in increasing the EM field enhancement. A similar study was conducted by Zhou *et al.* [60], who prepared Ag nanorod SERS substrates by OAD and GLAD at $T = 233$ K and 393 K. Their study has revealed that LT deposition results in well-separated nanorods with smaller diameter and also greatly improves the SERS activity.

Besides the tilted AgNR substrates, more complicated Ag nanostructures are developed to further improve the SERS activity by creating more "hot spots" on surface. Many studies have demonstrated that the "hot spots" are usually topological singularities on metallic surfaces, such as corners [61, 62]. Corners or "hot spots" can be created by bending the nanorods, which can be realized by rotating the substrates between two consecutive OAD depositions. The SERS activities of the bent AgNRs have been investigated by a series of studies conducted by Zhou *et al.* [51, 52, 54]. L-shaped nanorod arrays (bending number $N_b = 1$), as shown in Fig. 7(a), can be fabricated by azimuthally rotating the substrate by 180° during the OAD deposition [52]. By repeating such a process multiple times, zig-zag nanorod arrays ($N_b > 1$) can be fabricated [54]. Figures 7(b)–(d) show the SEM images of Ag zig-zag nanorods with $N_b = 3$, 5, and 7, respectively. In order to study how N_b affects the SERS activity, the SERS intensities of R6G 611 cm^{-1} Raman peak from a group of Ag zig-zag nanorods with the same total nanorod length but different N_b (0–7) are compared and plotted in Fig. 7(e). It is found the SERS activity increases with N_b when $N_b \leqslant 4$ but decreases when $N_b > 4$. The increase in SERS activity is believed to be the contribution from more "hot spots" generated by bending the nanorods, while the decrease in SERS activity may result from the longitudinal LSPR wavelength shifting away from the excitation wavelength (785 nm) due to the small aspect ratio of Ag arms with $N_b > 4$. Thus the maximum SERS response is achieved at $N_b = 4$ and almost three times as high as that of the tilted AgNR arrays. Further, if the substrate is azimuthally rotated by 90° between two consecutive depositions, a three dimensional (3D) square helical AgNRs can be fabricated as shown in Fig. 8(a). The length of each arm is fixed at about 760 nm. Figure 8(b) shows the dependence of SERS signal on the bending number N_b. When $N_b < 5$, the SERS activity increases rapidly with N_b, which primarily originates from the contribution of more "hot spots". When $N_b > 5$, the SERS activity increases slowly with N_b. Although the total number of "hot spots" still increases with N_b, the "hot spots" at the bottom of the structures make less or no contribution to the SERS signal, because the top layers attenuate both the incident light and scattered light.

4 Surface-enhanced infrared absorption

SEIRA has been developed as a sensitive detection technique. Similar to SERS, the enhanced localized EM field generated by LSPR excitation plays a significant role in improving the IR signals of the molecules in close proximity to the surfaces of metallic nanostructures. The enhancement of IR signals can be as high as 1000 and thus improving the detection sensitivity [9]. Besides the high sensitivity, another advantage of SEIRA is to shorten measurement time, especially when compared with the conventional infrared reflection-absorption spectroscopy (IRAS).

Thin films composed of island structures have been widely used as substrates for SEIRA measurements. These films are usually fabricated by physical vapor deposition at normal incidence ($\theta = 0°$). It has been shown

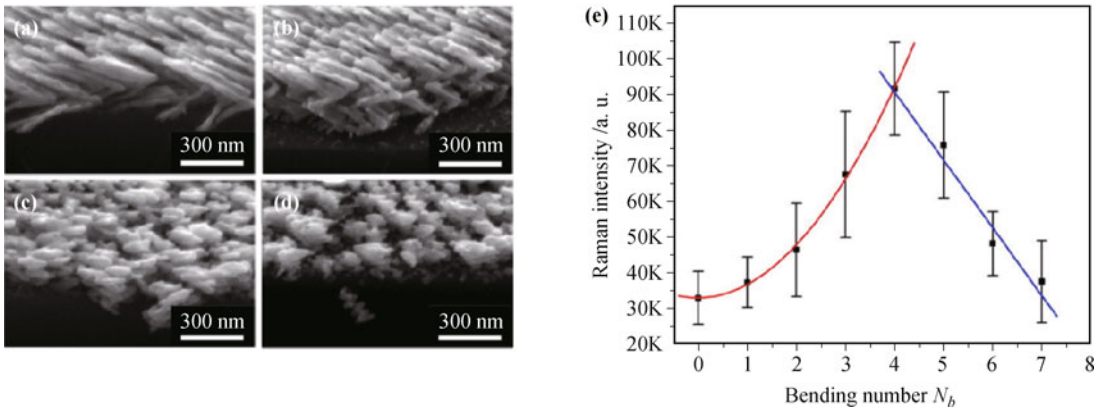

Fig. 7 **(a)–(d)** Cross-sectional SEM images of zigzag AgNRs with $N_b = 1$, 3, 5, and 7, respectively. **(e)** SERS intensity of R6G as a function of bending number N_b at Raman shift $\Delta\nu = 611$ cm^{-1} obtained on zig-zag AgNR arrays. Reproduced from Ref. [54], Copyright © 2012 American Institute of Physics.

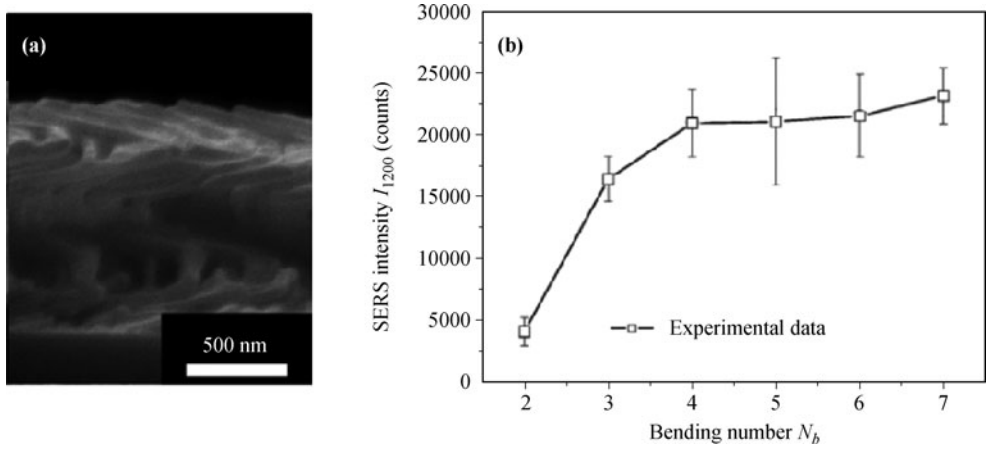

Fig. 8 **(a)** Cross-sectional SEM image of square helical nanorods with $N_b = 6$, and **(b)** dependence of I_{1200} on bending number N_b. Reproduced from Ref. [51], Copyright © 2011 Royal Society of Chemistry.

that the enhancement of IR signals strongly depends on the shape and size of islands, which are affected by the deposition parameters, such as the deposition rate, the thickness of film, and the substrate temperature [63]. However, the NP thin films fabricated by physical vapor deposition at normal incidence usually have a large variation of particle size, which leads to a poor uniformity of IR signal.

Because of the similarity between the mechanisms of SERS and SEIRA, it is reasonable to believe that the AgNR array prepared by OAD should also be a good SEIRA substrate. The optimal AgNR arrays fabricated by OAD were evaluated for the SEIRA performance by Leverette et al. using the probe molecule paranitrobenzoic acid (PNBA) [56]. As a reference, Ag thin film with thickness of 500 nm was used as standard substrates for IRAS. Figures 9(a) and (b) show the SEIRA and IRAS spectra of PNBA that were collected in the external reflection geometry, respectively. The band at 1410 cm^{-1} is assigned to the symmetric COO- stretching mode and the other band at 1350 cm^{-1} is assigned to the symmetric NO_2 stretching mode [64]. The peak intensity of the latter one was used to calculate the overall enhancement factor for SEIRA over IRAS, which was about 31±9. The enhancement factor is not as high as the one reported by Osawa [65], but is still very significant.

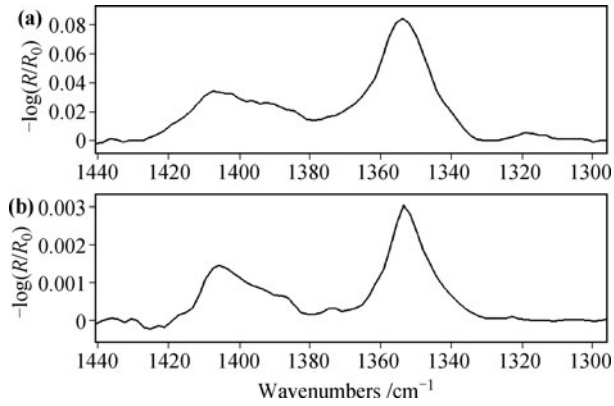

Fig. 9 **(a)** External reflection SEIRA spectrum (32 scans) of 1.67 μg PNBA on a Ag nanorod (average nanorod length = 868 nm) substrate, and **(b)** IRRAS spectrum (500 scans) of PNBA on a 500 nm Ag thin film substrate. Reproduced from Ref. [56], Copyright © 2006 Society for Applied Spectroscopy.

5 Metal-enhanced fluorescence

MEF is a phenomenon where the fluorescence intensity can dramatically increase when fluorophores are near the metallic surfaces, and has been observed and reported intensively in recent years [11–13]. The enhancement of fluorescence intensity primarily originates from the enhanced localized EM field generated by LSPR, and can greatly improve the radiative decay rates of the adsorbed molecules.

MEF based on Ag nanostructures made by OAD and GLAD has been demonstrated. The experiment process was the following: Si nanorods with a normal thickness of 2000 nm were firstly fabricated by GLAD. Then Ag of more than 15nm was deposited on the top of Si nanorods at $\theta = 45°$, as shown in Fig. 10(a). The tilted short Ag rods are sitting on top of the Si nanorods. As a comparison, a thin layer of Au (15 nm) was deposited on another piece of Si nanorods, shown in Fig. 10(b). To observe the MEF effect, the Si surface was coated with Fluorescein isothiocyanate (FITC) and its fluorescence intensity on Ag/Si nanorods and on Au/Si nanorods were measured quantitatively. Figures 10(c) and (d) show the cross section of SEM images of Ag/Si nanorods and Au/Si nanorods after FITC immobilization onto Si surface. The insets are corresponding confocal microscopy images after FITC immo-

bilization. It shows that, after the solution treatments, the Au/Si nanorods are bundled, while Ag nanostructures in Ag/Si nanorods fall into the gap between the Si nanorods. According to the confocal images, the signal from Au/Si nanorods/FITC is weak [dark appearance in Fig. 10(d)], while Ag/Si nanorods/FITC almost turns to white due to the intensity saturation. Using Typhon Scanner (488 nm excitation) to quantitatively evaluate the intensity of these samples, the integration of the intensity is 358 and 5410 for Au/Si nanorods/FITC and Ag/Si nanorods/FITC, respectively. Impressively, the intensity of Ag/Si nanorods/FITC increases by 15 folds. It has been reported that, if the fluorophores are located 5–10 nm away from the metallic surface, the fluorescence intensity will be greatly enhanced [66]. Therefore, the increased fluorescence intensity is caused by the interaction between the FITC coated on Si nanorods and the Ag nanostructures distributed either on the top or between the Si nanorods.

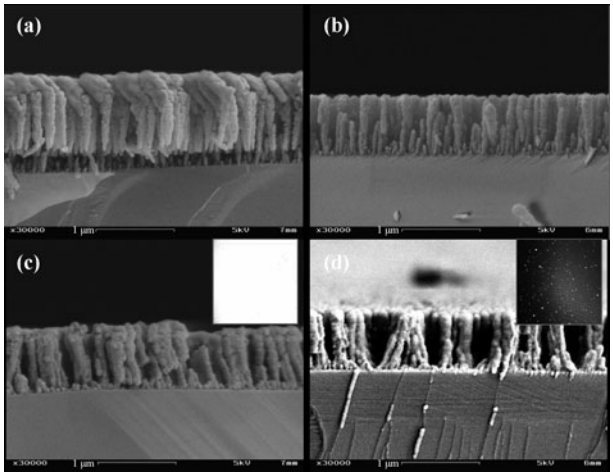

Fig. 10 SEM cross sections of Ag/Si nanorods **(a)** before and **(c)** after FITC immobilization onto Si surface. SEM cross sections of Au/Si nanorods **(b)** before and **(d)** after FITC immobilization onto Si surface. The insets are corresponding confocal microscopy images after FITC immobilization.

MEF effect based on OAD nanostructures has been applied to bacteria imaging by Abdulhalim *et al.* [67]. For MEF measurements, Ag nanorods, Ag film, Al nanorods, and Al film prepared by OAD were spin coated with the fluorescent dye Rhodamine 123 diluted in methanol at 0.6 wt%. The thickness of the dye layer was estimated by AFM to be 50 nm. The enhancement factors for the nanorods with respect to the corresponding reference film were compared. Figure 11(a) shows the fluorescence spectra of Ag and Al nanorods together with that of their reference samples, Ag and Al films. The ratio between the peaks at 590 nm gives enhancement factors of 15 for Ag nanorods and 11 for Al nanorods. The insert in Fig. 11(a) is the SEM image of Ag nanorods showing the highest enhancement. To demonstrate bio-imaging, the AgNRs and Ag film chips were inserted in an aqueous solution of *E. coli* with a concentration of 3.6×10^8 cfu/mL to observe the fluorescence from the bacteria. As shown in Figs. 11(b) and (c), undoubtedly, the Ag nanorods exhibit MEF to a higher degree than the reference film. The researchers believed that local field plasmon enhancement effects might be the main contributor. In addition, the nanorods are separated by few nanometers to a few tens of nanometers and the dipole-dipole interaction can play a major role in the enhancement mechanism [66, 68].

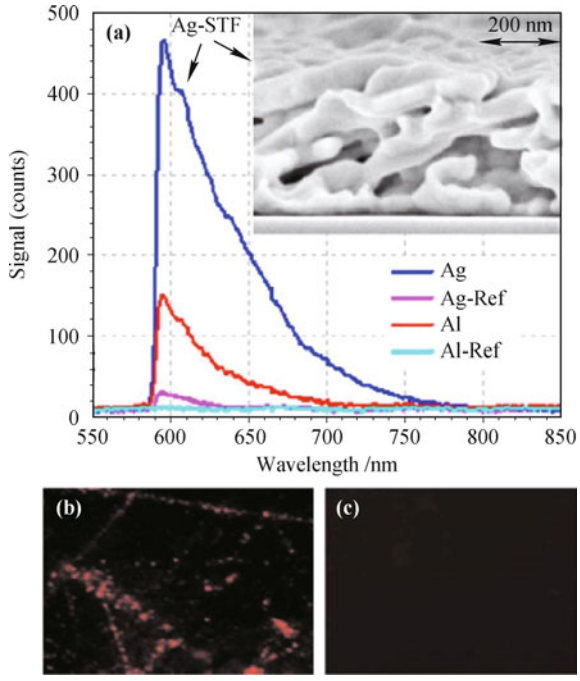

Fig. 11 **(a)** Typical fluorescence spectra from a Ag-nanorod film and an Al-nanorod film, and from the corresponding reference films. *Inset*: SEM image of Ag nanorod film showing the highest enhancement factor. Fluorescence images from **(b)** Ag-nanorod STF, and **(c)** a dense Ag film immersed in an aqueous solution of luminescent *E. coli*. Reproduced from Ref. [67], Copyright © 2009 American Institute of Physics.

6 Metamaterials

Metamaterials are the artificial composite materials possessing unique optical properties usually not observed in nature [14]. Metamaterials consist of large numbers of unit structures, which are usually made of metal or dielectric materials, periodically distributed and smaller than the wavelength being considered. The primary factors determining the property of metamaterials are the size, shape, orientation, and arrangement of the unit

structures, instead of the composition materials.

One of the exciting properties of metamaterial is the negative refractive index, which has been discussed thoroughly in other reviews [14, 69]. When a composite material with permittivity $\varepsilon = \varepsilon' + i\varepsilon''$and permeability $\mu = \mu' + i\mu''$ have both negative ε'andμ', or satisfy the inequality $\varepsilon'\mu'' + \mu'\varepsilon'' < 0$ for a passive medium, the refractive index of this material $n = n' + in''$ will have a negative real part n'. The negative index of refraction has been realized by various design of structures such as split ring resonators (SRRs) [70] and fishnet structure [25, 71]. Recently, the parallel metallic nanorod arrays exhibit negative index of refraction in visible-near infrared region [24, 72]. OAD is one of the methods to be able to fabricate the parallel nanorod arrays and thus can be applied in the fabrication of negative refractive metamaterials. Jen *et al.* has demonstrated that the titled AgNR array fabricated by OAD has negative index of refraction [20]. In their work, the tilting angle β of AgNRs was about 66°, and the average length and diameter are 650 nm and 80 nm, respectively. The refractive indices of the AgNR thin films were derived using both the transmission and reflection coefficients at different wavelengths (532, 639 and 690 nm), measured by ellipsometry and interferometry, and were found to be $n' =$ –0.705, –0.476, –0.552 at the wavelength of 532, 639, 690 nm respectively for *p*-polarized normally incident light. Later studies by the same group show that the negative real refractive index can be varied by changing the morphology of AgNRs, such as changing the length and tilting angle [73] and bending the nanorods to form L-shaped or Z-shaped nanostructures [74]. In addition, a negative real permeability can also be achieved by increasing the nanorod length, which is attributed to the effect of the inverse magnetic field [75]. However, the AgNR arrays usually have very low transmission in visible region (< 1%) for *p*-polarized incident light. In order to improve the transmission, a $Ag/SiO_2/Ag$ sandwich nanostructure was fabricated by GLAD [76]. As shown in Figs. 12(a) and (b), a 70 nm thick SiO_2 segment is deposited between two 120 nm thick Ag nanorod segments. The top view SEM image also reveals no anisotropic feature of the sandwich structure due to the fast rotation of substrates during the deposition, which leads to isotropic optical parameters. As shown in Fig. 12(c), the $Ag/SiO_2/Ag$ sandwich structure exhibits negative real refractive indices in the wavelength range 476–690 nm with improved optical transmission. The transmission of the sandwich ranges from 3.62% to 17.32% in visible region, which is larger than that of AgNR arrays.

Chiral structures, as a way to obtain negative index of refraction [77], also exhibits strong chiroptical behavior such as optical activity and circular dichroism, and has been developed rapidly [78–83]. Recently, the fabrication of the chiral metamaterials by GLAD method has been realized by Gallas *et al.* [84, 85]. In their work, 3D square helical nanostructures of Ag with $N_b = 2$ were fabricated and generalized spectroscopic ellipsometry measurements revealed the conversion between polarization states.

Although OAD and GLAD techniques have demonstrated some success in fabricating metamaterials, large numbers of disorders and defects exist in the samples and limit their application in metamaterials. Future work should aim to minimize these disorders and defects.

7 Conclusion

We have reviewed the recent progress on the plasmonic applications of metallic nanostructures fabricated by OAD and GLAD techniques, which are capable of producing versatile nanomaterials, such as Ag and Au nanoparticles, tilted AgNRs, L-shaped, zig-zag and square helical AgNRs. These metallic nanostructures exhibit good or enhanced sensitivity in LSPR sensing, SERS, SEIRA and MEF, provide practical applications in monitoring the interaction between molecules and

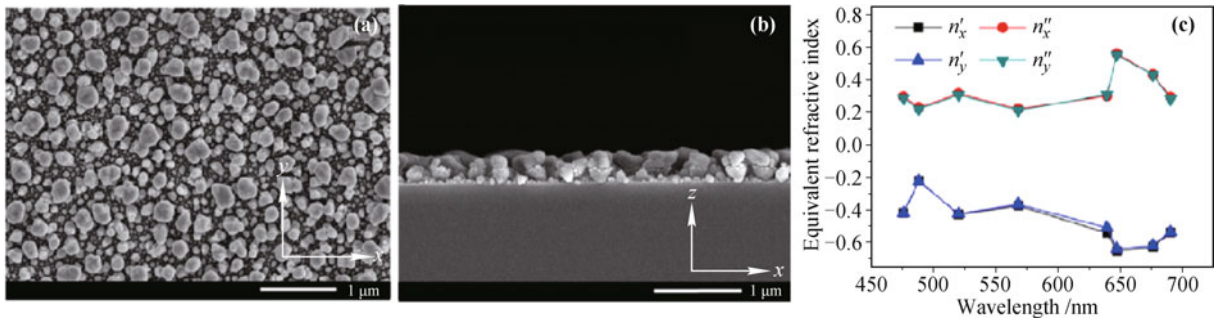

Fig. 12 **(a)** Top-view and **(b)** cross-sectional SEM image of the $Ag/SiO_2/Ag$ sandwich structure. **(c)** Measured real and imaginary parts of refractive indices of the sandwich structure with different polarized incident light. Reproduced from Ref. [76], Copyright © 2011 American Institute of Physics.

protein, recognizing molecules, detecting RNAs, viruses, and bacteria, and bio-imaging. There is still a lot of space left for further sensitivity improvement, especially to tune the size and shape of the nanostructure and make the structure more uniform. Novel negative refractive index property is also found in the parallel AgNR arrays and chiral Ag square helix. In our opinion, these metamaterial made by OAD and GLAD will offer great opportunities in making unique optical devices, provided that the disorders and defects in the nanostructure arrays can be minimized. In a word, the effective use of OAD and GLAD techniques can result in more novel applications in the field of plasmonics.

Acknowledgements Y. Z. He and Y. P. Zhao are supported by the National Science Foundation under the Contract Number ECCS-1029609. J. X. Fu is supported by Hong Kong Baptist University RC-start up grant 38-40-065.

References

1. B. Rodriguez-Gonzalez, A. Burrows, M. Watanabe, C. J. Kiely, and L. M. L. Marzan, Multishell bimetallic AuAg nanoparticles: Synthesis, structure and optical properties, *J. Mater. Chem.*, 2005, 15(17): 1755
2. M. M. Miller and A. A. Lazarides, Sensitivity of metal nanoparticle surface plasmon resonance to the dielectric environment, *J. Phys. Chem. B*, 2005, 109(46): 21556
3. C. Burda, X. B. Chen, R. Narayanan, and M. A. El-Sayed, Chemistry and properties of nanocrystals of different shapes, *Chem. Rev.*, 2005, 105(4): 1025
4. H. X. Li and L. Rothberg, Colorimetric detection of DNA sequences based on electrostatic interactions with unmodified gold nanoparticles, *Proc. Natl. Acad. Sci. USA*, 2004, 101(39): 14036
5. N. L. Rosi and C. A. Mirkin, Nanostructures in biodiagnostics, *Chem. Rev.*, 2005, 105(4): 1547
6. D. Cialla, A. März, R. Böhme, F. Theil, K. Weber, M. Schmitt, and J. Popp, Surface-enhanced Raman spectroscopy (SERS): Progress and trends, *Anal. Bioanal. Chem.*, 2012, 403(1): 27
7. P. Negri and R. A. Dluhy, Ag nanorod based surface-enhanced Ramanspectroscopy applied to bioanalytical sensing, *J. Biophotonics*, 2013, 6: 20
8. B. Sharma, R. R. Frontiera, A. I. Henry, E. Ringe, and R. P. Van Duyne, SERS: Materials, applications, and the future, *Mater. Today*, 2012, 15(1–2): 16
9. R. F. Aroca, D. J. Ross, and C. Domingo, Surface-enhanced infrared spectroscopy, *Appl. Spectrosc.*, 2004, 58(11): 324A
10. M. Osawa, Dynamic processes in electrochemical reactions studied by surface-enhanced infrared absorption spectroscopy (SEIRAS), *Bull. Chem. Soc. Jpn.*, 1997, 70(12): 2861
11. N. Bondre, Y. X. Zhang, and C. D. Geddes, Metal-enhanced fluorescence based calcium detection: Greater than 100-fold increase in signal/noise using Fluo-3 or Fluo-4 and silver nanostructures, *Sens. Actuators B*, 2011, 152(1): 82
12. R. Nooney, A. Clifford, X. Leguevel, O. Stranik, C. McDonagh, and B. D. Maccraith, Enhancing the analytical performance of immunoassays that employ metal-enhanced fluorescence, *Anal. Bioanal. Chem.*, 2010, 396(3): 1127
13. A. I. Dragan, E. S. Bishop, J. R. Casas-Finet, R. J. Strouse, M. A. Schenerman, and C. D. Geddes, Metal-enhanced PicoGreen fluorescence: Application to fast and ultra-sensitive pg/ml DNA quantitation, *J. Immunol. Methods*, 2010, 362(1–2): 95
14. Y. Liu and X. Zhang, Metamaterials: A new frontier of science and technology, *Chem. Soc. Rev.*, 2011, 40(5): 2494
15. T. Tanaka, Plasmonic metamaterials, *IEICE Electron. Express*, 2012, 9(2): 34
16. X. Z. Zhou, F. Boey, F. W. Huo, L. Huang, and H. Zhang, Chemically functionalized surface patterning, *Small*, 2011, 7(16): 2273
17. Z. H. Xie, W. X. Yu, T. S. Wang, H. X. Zhang, Y. Q. Fu, H. Liu, F. Y. Li, Z. W. Lu, and Q. Sun, Plasmonic nanolithography: A review, *Plasmonics*, 2011, 6(3): 565
18. R. G. Freeman, K. C. Grabar, K. J. Allison, R. M. Bright, J. A. Davis, A. P. Guthrie, M. B. Hommer, M. A. Jackson, P. C. Smith, D. G. Walter, and M. J. Natan, Self-assembled metal colloid monolayers: An approach to SERS substrates, *Science*, 1995, 267(5204): 1629
19. Y. J. Liu, H. Y. Chu, and Y. P. Zhao, Silver nanorod array substrates fabricated by oblique angle deposition: Morphological, optical, and SERS characterizations, *J. Phys. Chem. C*, 2010, 114(18): 8176
20. Y. J. Jen, A. Lakhtakia, C. W. Yu, and C. T. Lin, Vapor-deposited thin films with negative real refractive index in the visible regime, *Opt. Express*, 2009, 17(10): 7784
21. K. Robbie, J. C. Sit, and M. J. Brett, Advanced techniques for glancing angle deposition, *J. Vac. Sci. Technol. B*, 1998, 16(3): 1115
22. M. Kahl, E. Voges, S. Kostrewa, C. Viets, and W. Hill, Periodically structured metallic substrates for SERS, *Sens. Actuators B*, 1998, 51(1–3): 285
23. N. A. Abu Hatab, J. M. Oran, and M. J. Sepaniak, Surface-enhanced Raman spectroscopy substrates created via electron beam lithography and nanotransfer printing, *ACS Nano*, 2008, 2(2): 377
24. V. M. Shalaev, W. S. Cai, U. K. Chettiar, H. K. Yuan, A. K. Sarychev, V. P. Drachev, and A. V. Kildishev, Negative index of refraction in optical metamaterials, *Opt. Lett.*, 2005, 30(24): 3356
25. S. M. Xiao, U. K. Chettiar, A. V. Kildishev, V. P. Drachev, and V. M. Shalaev, Yellow-light negative-index metamaterials, *Opt. Lett.*, 2009, 34(22): 3478
26. J. C. Hulteen, D. A. Treichel, M. T. Smith, M. L. Duval, T. R. Jensen, and R. P. Van Duyne, Nanosphere lithography:

Size-tunable silver nanoparticle and surface cluster arrays, *J. Phys. Chem. B*, 1999, 103(19): 3854

27. C. L. Haynes and R. P. Van Duyne, Nanosphere lithography: A versatile nanofabrication tool for studies of size-dependent nanoparticle optics, *J. Phys. Chem. B*, 2001, 105(24): 5599
28. A. D. Ormonde, E. C. M. Hicks, J. Castillo, and R. P. Van Duyne, Nanosphere lithography: Fabrication of large-area Ag nanoparticle arrays by convective self-assembly and their characterization by scanning UV-visible extinction spectroscopy, *Langmuir*, 2004, 20(16): 6927
29. L. Abelmann and C. Lodder, Oblique evaporation and surface diffusion, *Thin Solid Films*, 1997, 305(1–2): 1
30. H. Vankranenburg and C. Lodder, Tailoring growth and local composition by oblique-incidence deposition: A review and new experimental data, *Mater. Sci. Eng. R*, 1994, 11(7): 295
31. K. Robbie and M. J. Brett, Sculptured thin films and glancing angle deposition: Growth mechanics and applications, *J. Vac. Sci. Technol. A*, 1997, 15(3): 1460
32. Y. P. Zhao, D. X. Ye, G. C. Wang, and T. M. Lu, Novel nano-column and nano-flower arrays by glancing angle deposition, *Nano Lett.*, 2002, 2(4): 351
33. Y. P. He and Y. P. Zhao, Advanced multi-component nanostructures designed by dynamic shadowing growth, *Nanoscale*, 2011, 3(6): 2361
34. J. X. Fu, Y. P. He, and Y. P. Zhao, Fabrication of heteronanorod structures by dynamic shadowing growth, *IEEE Sens. J.*, 2008, 8(6): 989
35. Y. P. He, Z. Y. Zhang, C. Hoffmann, and Y. P. Zhao, Embedding Ag nanoparticles into MgF_2 nanorod arrays, *Adv. Funct. Mater.*, 2008, 18(11): 1676
36. Y. P. He, Y. P. Zhao, and J. S. Wu, The effect of Ti doping on the growth of Mg nanostructures by oblique angle codeposition, *Appl. Phys. Lett.*, 2008, 92(6): 063107
37. Y. P. He, C. Brown, C. A. Lundgren, and Y. P. Zhao, The growth of CuSi composite nanorod arrays by oblique angle co-deposition, and their structural, electrical and optical properties, *Nanotechnology*, 2012, 23(36): 365703
38. G. K. Larsen, R. Fitzmorris, J. Z. Zhang, and Y. P. Zhao, Structural, optical, and photocatalytic properties of Cr:TiO_2 nanorod array fabricated by oblique angle codeposition, *J. Phys. Chem. C*, 2011, 115(34): 16892
39. G. K. Larsen, B. C. Fitzmorris, C. Longo, J. Z. Zhang, and Y. P. Zhao, Nanostructured homogenous CdSe-TiO_2 composite visible light photoanodes fabricated by oblique angle codeposition, *J. Mater. Chem.*, 2012, 22(28): 14205
40. Y. P. He, J. S. Wu, and Y. P. Zhao, Designing catalytic nanomotors by dynamic shadowing growth, *Nano Lett.*, 2007, 7(5): 1369
41. Y. P. He, J. X. Fu, Y. Zhang, Y. P. Zhao, L. J. Zhang, A. L. Xia, and J. W. Cai, Multilayered Si/Ni nanosprings and their magnetic properties, *Small*, 2007, 3(1): 153
42. W. Smith and Y. P. Zhao, Enhanced photocatalytic activity by aligned WO_3/TiO_2 two-layer nanorod arrays, *J. Phys. Chem. C*, 2008, 112(49): 19635
43. W. Smith and Y. P. Zhao, Superior photocatalytic performance by vertically aligned core-shell TiO_2/WO_3 nanorod arrays, *Catal. Commun.*, 2009, 10(7): 1117
44. R. Gupta, M. J. Dyer, and W. A. Weimer, Preparation and characterization of surface plasmon resonance tunable gold and silver films, *J. Appl. Phys.*, 2002, 92(9): 5264
45. J. X. Fu, A. Collins, and Y. P. Zhao, Optical properties and biosensor application of ultrathin silver films prepared by oblique angle deposition, *J. Phys. Chem. C*, 2008, 112(43): 16784
46. J. X. Fu and Y. P. Zhao, Au nanoparticle based localized surface plasmon resonance substrates fabricated by dynamic shadowing growth, *Nanotechnology*, 2010, 21(17): 175303
47. D. A. Gish, F. Nsiah, M. T. McDermott, and M. J. Brett, Localized surface plasmon resonance biosensor using silver nanostructures fabricated by glancing angle deposition, *Anal. Chem.*, 2007, 79(11): 4228
48. D. R. H. Craig and F. Bohren, Absorption and scattering of light by small particles, New York: Wiley, 1983
49. U. Kreibig and M. Vollmer, Optical Properties of Metal Clusters, Berlin: Springer, 1995
50. J. D. Driskell, S. Shanmukh, Y. Liu, S. B. Chaney, X. J. Tang, Y. P. Zhao, and R. A. Dluhy, The use of aligned silver nanorod arrays prepared by oblique angle deposition as surface enhanced raman scattering substrates, *J. Phys. Chem. C*, 2008, 112(4): 895
51. Q. Zhou, Y. He, J. Abell, Z. Zhang, and Y. Zhao, Surface-enhanced Raman scattering from helical silver nanorod arrays, *Chem. Commun.*, 2011, 47(15): 4466
52. Q. Zhou, Y. He, J. Abell, Z. Zhang, and Y. Zhao, Optical properties and surface enhanced raman scattering of L-shaped silver nanorod arrays, *J. Phys. Chem. C*, 2011, 115(29): 14131
53. J. P. Singh, T. E. Lanier, H. Zhu, W. M. Dennis, R. A. Tripp, and Y. Zhao, Highly sensitive and transparent surface enhanced Raman scattering substrates made by active coldly condensed Ag nanorod arrays, *J. Phys. Chem. C*, 2012, 116(38): 20550
54. Q. Zhou, X. Zhang, Y. Huang, Z. Li, Y. Zhao, and Z. Zhang, Enhanced surface-enhanced Raman scattering performance by folding silver nanorods, *Appl. Phys. Lett.*, 2012, 100(11): 113101
55. S. B. Chaney, S. Shanmukh, R. A. Dluhy, and Y. P. Zhao, Aligned silver nanorod arrays produce high sensitivity surface-enhanced Raman spectroscopy substrates, *Appl. Phys. Lett.*, 2005, 87(3): 031908
56. C. L. Leverette, S. A. Jacobs, S. Shanmukh, S. B. Chaney, R. A. Dluhy, and Y. P. Zhao, Aligned silver nanorod arrays as substrates for surface-enhanced infrared absorption spectroscopy, *Appl. Spectrosc.*, 2006, 60(8): 906
57. J. L. Abell, J. M. Garren, and Y. P. Zhao, Dynamic rastering surface-enhanced Raman scattering (SERS) measurements on silver nanorod substrates, *Appl. Spectrosc.*, 2011, 65(7): 734

58. C. M. Ruan, G. Eres, W. Wang, Z. Y. Zhang, and B. H. Gu, Controlled fabrication of nanopillar arrays as active substrates for surface-enhanced Raman spectroscopy, *Langmuir*, 2007, 23(10): 5757
59. M. A. De Jesús, K. S. Giesfeldt, J. M. Oran, N. A. Abu-Hatab, N. V. Lavrik, and M. J. Sepaniak, Nanofabrication of densely packed metal-polymer arrays for surface-enhanced Raman spectrometry, *Appl. Spectrosc.*, 2005, 59(12): 1501
60. Q. Zhou, Z. Li, Y. Yang, and Z. Zhang, Arrays of aligned, single crystalline silver nanorods for trace amount detection, *J. Phys. D*, 2008, 41(15): 152007
61. L. D. Qin, S. L. Zou, C. Xue, A. Atkinson, G. C. Schatz, and C. A. Mirkin, Designing, fabricating, and imaging Raman hot spots, *Proc. Natl. Acad. Sci. USA*, 2006, 103(36): 13300
62. S. L. Kleinman, R. R. Frontiera, A. I. Henry, J. A. Dieringer, and R. P. Van Duyne, Creating, characterizing, and controlling chemistry with SERS hot spots, *Phys. Chem. Chem. Phys.*, 2013, 15(1): 21
63. Y. Nishikawa, T. Nagasawa, K. Fujiwara, and M. Osawa, Silver island films for surface-enhanced infrared absorption spectroscopy: Effect of island morphology on the absorption enhancement, *Vib. Spectrosc.*, 1993, 6(1): 43
64. M. Osawa and M. Ikeda, Surface-enhanced infrared absorption of p-nitrobenzoic acid deposited on silver island films: contributions of electromagnetic and chemical mechanisms, *J. Phys. Chem.*, 1991, 95(24): 9914
65. Y. Nishikawa, K. Fujiwara, K. Ataka, and M. Osawa, Surface-enhanced infrared external reflection spectroscopy at low reflective surfaces and its application to surface analysis of semiconductors, glasses, and polymers, *Anal. Chem.*, 1993, 65(5): 556
66. J. R. Lakowicz, C. D. Geddes, I. Gryczynski, J. Malicka, Z. Gryczynski, K. Aslan, J. Lukomska, E. Matveeva, J. A. Zhang, R. Badugu, and J. Huang, Advances in surface-enhanced fluorescence, *J. Fluoresc.*, 2004, 14(4): 425
67. I. Abdulhalim, A. Karabchevsky, C. Patzig, B. Rauschenbach, B. Fuhrmann, E. Eltzov, R. Marks, J. Xu, F. Zhang, and A. Lakhtakia, Surface-enhanced fluorescence from metal sculptured thin films with application to biosensing in water, *Appl. Phys. Lett.*, 2009, 94(6): 063106
68. H. R. Stuart and D. G. Hall, Enhanced dipole-dipole interaction between elementary radiators near a surface, *Phys. Rev. Lett.*, 1998, 80(25): 5663
69. W. J. Padilla, D. N. Basov, and D. R. Smith, Negative refractive index metamaterials, *Mater. Today*, 2006, 9(7–8): 28
70. J. B. Pendry, A. J. Holden, D. J. Robbins, and W. J. Stewart, Magnetism from conductors and enhanced nonlinear phenomena, *IEEE Trans. Microw. Theory Tech.*, 1999, 47(11): 2075
71. S. Zhang, W. J. Fan, N. C. Panoiu, K. J. Malloy, R. M. Osgood, and S. R. J. Brueck, Experimental demonstration of near-infrared negative-index metamaterials, *Phys. Rev. Lett.*, 2005, 95(13): 137404
72. J. Yao, Z. W. Liu, Y. M. Liu, Y. Wang, C. Sun, G. Bartal, A. M. Stacy, and X. Zhang, Optical negative refraction in bulk metamaterials of nanowires, *Science*, 2008, 321(5891): 930
73. Y. J. Jen, C. H. Chen, and C. W. Yu, Deposited metamaterial thin film with negative refractive index and permeability in the visible regime, *Opt. Lett.*, 2011, 36(6): 1014
74. Y. J. Jen, A. Lakhtakia, C. W. Yu, and Y. H. Wang, Negative real parts of the equivalent permittivity, permeability, and refractive index of sculptured-nanorod arrays of silver, *J. Vac. Sci. Technol. A*, 2010, 28(5): 1078
75. A. N. Lagarkov and A. K. Sarychev, Electromagnetic properties of composites containing elongated conducting inclusions, *Phys. Rev. B*, 1996, 53(10): 6318
76. Y. J. Jen, A. Lakhtakia, C. W. Yu, J. J. Jhou, W. H. Wang, M. J. Lin, H. M. Wu, and H. S. Liao, Silver/silicon dioxide/silver sandwich films in the blue-to-red spectral regime with negative-real refractive index, *Appl. Phys. Lett.*, 2011, 99(18): 181117
77. E. Plum, J. Zhou, J. Dong, V. A. Fedotov, T. Koschny, C. M. Soukoulis, and N. I. Zheludev, Metamaterial with negative index due to chirality, *Phys. Rev. B*, 2009, 79(3): 035407
78. A. Papakostas, A. Potts, D. M. Bagnall, S. L. Prosvirnin, H. J. Coles, and N. I. Zheludev, Optical manifestations of planar chirality, *Phys. Rev. Lett.*, 2003, 90(10): 107404
79. M. Decker, M. W. Klein, M. Wegener, and S. Linden, Circular dichroism of planar chiral magnetic metamaterials, *Opt. Lett.*, 2007, 32(7): 856
80. A. V. Rogacheva, V. A. Fedotov, A. S. Schwanecke, and N. I. Zheludev, Giant gyrotropy due to electromagnetic-field coupling in a bilayered chiral structure, *Phys. Rev. Lett.*, 2006, 97(17): 177401
81. M. Decker, M. Ruther, C. E. Kriegler, J. Zhou, C. M. Soukoulis, S. Linden, and M. Wegener, Strong optical activity from twisted-cross photonic metamaterials, *Opt. Lett.*, 2009, 34(16): 2501
82. M. Kuwata-Gonokami, N. Saito, Y. Ino, M. Kauranen, K. Jefimovs, T. Vallius, J. Turunen, and Y. Svirko, Giant optical activity in quasi-two-dimensional planar nanostructures, *Phys. Rev. Lett.*, 2005, 95(22): 227401
83. M. Decker, R. Zhao, C. M. Soukoulis, S. Linden, and M. Wegener, Twisted split-ring-resonator photonic metamaterial with huge optical activity, *Opt. Lett.*, 2010, 35(10): 1593
84. B. Gallas, K. Robbie, R. Abdeddaïm, G. Guida, J. Yang, J. Rivory, and A. Priou, Silver square nanospirals mimic optical properties of U-shaped metamaterials, *Opt. Express*, 2010, 18(16): 16335
85. B. Gallas, N. Guth, J. Rivory, H. Arwin, R. Magnusson, G. Guida, J. Yang, and K. Robbie, Nanostructured chiral silver thin films: A route to metamaterials at optical frequencies, *Thin Solid Films*, 2011, 519(9): 2650